Journal of Solid State Electrochemistry (2020) 24:389–399
https://doi.org/10.1007/s10008-020-04508-2

ORIGINAL PAPER

# Effect of the electrodeposition potential on the photoelectroactivity of the $SnS/Sb_2S_3$ thin films

Moisés A. de Araújo[1] · Francisco W. S. Lucas[2] · Lucia H. Mascaro[1]

Received: 30 September 2019 / Revised: 20 January 2020 / Accepted: 20 January 2020 / Published online: 30 January 2020


## Abstract

The present work outlines a simple and novel approach to obtain nanostructured and heterostructured $SnS/Sb_2S_3$ thin films. This material showed enhanced photoelectroactivity in comparison to the individual tin (II) sulphide (SnS) and antimony (III) sulphide ($Sb_2S_3$) films. These nanostructured films were grown by electrodeposition of antimony tin (SbSn) compound followed by sulphurisation under a sulphur vapour atmosphere. The optimisation of the growth methodology was systematically performed by evaluating the photoelectroactivity of the films prepared at different deposition potentials as well as by characterisation of the as-deposited binary compound and the films after sulphurisation. In comparison to the individual SnS and $Sb_2S_3$ films, the $SnS/Sb_2S_3$ one presented a photocurrent response increased 10-fold compared to the former and 48-fold compared to the latter. Further studies carried out by Mott-Schottky analysis and band gap determination confirmed that the band edge positions of the single SnS and $Sb_2S_3$ phases are suitably aligned, forming a type II heterostructure which facilitates minority carriers' separation and transportation and therefore improves the photocurrent density values.

**Keywords** Chalcogenide semiconductors · Photoelectrochemical cell · Water splitting · Tin sulphide · Antimony sulphide nanorods

## Introduction

Increasing petroleum consumption has raised concerns about its diminution over time and the environmental impacts that has caused. In light of the circumstances, alternative sustainable energy sources for the future have been sought to replace the current ones based on fossil fuels. The sun seems to meet humans' needs as the most abundant, renewable and inexhaustible source of energy for the Earth. It is estimated that $3 \times 10^{24}$ J of solar energy hit the earth annually; such amount of energy is 10,000 times higher than humankind currently requires [1].

In this context, technology using semiconductor materials in a photovoltaic cell (PVC) to convert solar energy into electricity as well as in a photoelectrochemical cell (PEC) to produce chemical energy shows promise for overcoming these energy issues. Additionally, due to economic and environmental appeals, semiconductors featuring earth-abundant and nontoxic fuels for the aforementioned application are highly in demand. Among the materials being studied, the sulpho-materials, such as SnS and $Sb_2S_3$, seem to meet the requirements [2–5].

SnS is natively a *p*-type semiconductor material having a high absorption coefficient ($\alpha$) of $> 10^4$ $cm^{-1}$ (for photons with energy higher than its band gap), an optical (allowed) direct and indirect band gap of 1.2–1.5 and 1.1 eV, respectively, and high charge carrier concentration (around $10^{17}$–$10^{18}$ $cm^{-3}$) [6]. Such features make this material a potential candidate to be applied as an absorber layer in PVCs [6, 7] or a photocathode in PECs [3, 8]. In terms of crystallographic structure, SnS belongs to the orthorhombic system (having a deformed NaCl structure) and has a peculiar structure

Dedicated to the memory of Ivo Alexandre Hümmelgen

**Electronic supplementary material** The online version of this article (https://doi.org/10.1007/s10008-020-04508-2) contains supplementary material, which is available to authorized users.

✉ Lucia H. Mascaro
lmascaro@ufscar.br

[1] Departamento de Química, Universidade Federal de São Carlos, Rodovia Washington Luiz, km 235, São Carlos, São Paulo 13565-905, Brazil

[2] Instituto de Química, Universidade de São Paulo, Avenida Trabalhador São Carlense, no. 400, São Carlos, São Paulo 3373-9900, Brazil

containing double layers of Sn and S, which are held together by weak Van der Waals interactions [7]. The presence of $SnS_2$ in the SnS photoactive bulk domain can be detrimental for PVC performance [9, 10]; notwithstanding this, studies have shown that the $SnS_2$ phase can be potentially beneficial as an *n*-type buffer layer [9]. In addition, such phase finds application in PEC for water splitting with a considerable photon-to-current conversion efficiency of 38.7% [10].

Along with SnS, $Sb_2S_3$ is as well considered a prospective material for solar harvesting energy applications due to its (allowed) direct and indirect band gap of 1.8–2.5 [11] and 1.6 eV [4], respectively, and a high $\alpha > 10^5$ $cm^{-1}$ (for photons with energy higher than its band gap) [12]. Additionally, $Sb_2S_3$ has an *n*-type or *p*-type electrical conductivity depending on its preparation method [13].

Several methodologies have been reported to synthesise thin films of SnS and $Sb_2S_3$, such as atomic layer deposition [14, 15], sputtering [16, 17], chemical vapour deposition [18, 19], thermal evaporation [5, 20], spray pyrolysis [21, 22] or chemical bath deposition [23, 24]. Another promising methodology is electrodeposition, which stands as an economic, simple, easily scalable and fast process for obtaining semiconductor thin films [6, 25, 26].

Despite electrodeposition's advantages, to the best of our knowledge, it has not been thoroughly explored for obtaining these materials so far. Most of the studies concerning the electrodeposition of SnS film evaluate the physical and optoelectronic properties as a function of the electrodeposition parameters [27, 28] as well as adding an electrodeposited dopant, e.g. selenium (Se) [29], zinc (Zn) [30] or aluminium (Al) [31]. Regarding the electrodeposition of $Sb_2S_3$ in literature, several electrochemical approaches, e.g. pulsed electrodeposition [32], an acid bath [33] and an alkaline bath [34], have been reported.

Concerning the application of these materials in PECs, several surface modifications and heterostructures, such as SnS/CdS/$TiO_2$/Pt [35], SnS/metal oxides [36], $CuInS_2$/$Sb_2S_3$/Pt [37] and $Sb_2O_3$/$Sb_2S_3$ [38], have been reported as enhancing photoactivity to hydrogen gas ($H_2$) production via water splitting. Although these additional layer materials have shown promise, no such attempt has previously endeavoured to obtain a new heterostructure system such as SnS/$Sb_2S_3$ for a solar harvesting application. Just recently, Bera et al. [39] reported a dual-layered and doped heterostructure material $Sn^{II}S$-$Sn^{IV}$:$Sb_2S_3$ for sodium ion storage.

Considering all of the aforementioned information, this work features a novel and simple way to obtain the nanostructured heterostructure SnS/$Sb_2S_3$ thin film via electrodeposition followed by sulphurisation under a sulphur vapour atmosphere. Additionally, the effect of the deposition's potential on the microstructure, morphology, optical properties and photoelectrochemical activity were evaluated.

## Experimental

### Chemicals

All the experiments were performed using chemicals of analytical grade, and no further purification was required. The main chemicals used were potassium antimony (III) tartrate, $K_2Sb_2(C_4H_2O_6)_2 \cdot xH_2O$ (Sigma-Aldrich, ≥ 99%); tin (II) chloride, $SnCl_2$ (Sigma-Aldrich, 98%); potassium sodium tartrate tetrahydrate, $KNa(C_4H_4O_6) \cdot 4H_2O$ (Sigma-Aldrich, ≥ 99%), elemental sulphur powder, S (Reagen), sodium sulphate, $Na_2SO_4$ (Synth, 99.0%) and 4-nitrophenol, $C_6H_5NO_3$ (Merck).

### Electrochemical characterisation and electrodeposition conditions

The electrochemical experiments were carried out on a potentiostat/galvanostat (Autolab PGSTAT302N) and an electrochemical cell designed in a three-electrode configuration containing a platinum plate (geometric area of ≈ 1.2 $cm^2$) as the counter electrode and an $Ag/AgCl/Cl^-_{(sat.\ KCl)}$ as the reference electrode. The working electrode, where the films were electrodeposited, was the fluorine-doped tin (IV) oxide (FTO, 7 Ω/sq., Sigma-Aldrich) coated glass substrate (geometric area of ≈ 0.5 $cm^2$). Before any experiments, the FTO was ultrasonically cleaned with deionised water, ethanol, acetone and isopropanol for 5 min in each solvent and thereupon hydrophilised for 1 h at 70 °C in a solution containing a volume ratio of 5:1:1 of $H_2O/H_2O_2$ (conc.)/$NH_4OH$ (conc.), respectively. Lastly, it was rinsed with deionised water and dried out with nitrogen gas stream.

The electrochemical behaviour of each solution was assessed using cyclic voltammetry (CV) on the FTO. The supporting electrolyte was 0.1 mol $L^{-1}$ $KNa(C_4H_4O_6)$ pH 6, which was adjusted by adding 0.1 mol $L^{-1}$ $H_2SO_4$. The precursor reagents $SnCl_2$, and $K_2Sb_2(C_4H_2O_6)_2$, with a molarity of 2 mmol $L^{-1}$ and 4 mmol $L^{-1}$, respectively, were dissolved in the supporting electrolyte. The CVs were scanned from the open circuit potential ($E_{ocp}$) towards a more negative potential at a scan rate of 20 mV $s^{-1}$. Based on the CVs' analysis, the potential depositions were selected to electrodeposit the films. All the films were electrodeposited with a charge density of −332 mC $cm^{-2}$.

### Sulphurisation condition

The electrodeposited films at different potential depositions were sulphurised under a sulphur vapour atmosphere at 270 °C for 3 h in a tubular furnace (EDGCON 5P) with heating and cooling rates of 10 and 1 °C $min^{-1}$, respectively. The sulphurisation setup as depicted in Fig. 1 consisted of a glass cylinder sealed by the friction of the two individual parts; inside of it was a silicon plate on which to place the

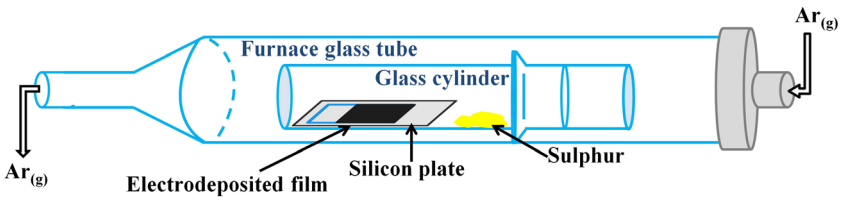


**Fig. 1** Sulphurisation setup for the electrodeposited films

films and 0.30 g of sulphur powder. The sealed glass tube was placed in a furnace glass tube with an argon (Ar) gas flux, and this system was optimised in our group [40, 41].

### Physical and chemical characterisation of the electrodeposited films

The unsulphured and sulphurised films obtained at different potential depositions were analysed in terms of their crystallographic structure using an X-ray diffractometer (Rigaku DMax 2500PC) with a Cu Kα radiation of 1.54 Å, which was produced at an acceleration voltage of 40 kV and a beam current of 30 mA. The diffractograms were obtained at a scan rate of 1.0° $min^{-1}$ and a step of 0.02°. A Raman spectrometer (Bruker Senterra) was also used for the microstructural analysis. A 532-nm laser operating at 5 mW of power was used as the excitation source. Each spectrum was collected with a resolution of 3–5 $cm^{-1}$ and an integration time of 5 s. The morphology analyses of the films were conducted on a scanning electron microscope (FEI-Inspect F50), and the chemical study was carried out on a SEM-FEG (Philips XL S30). In order to estimate the optical band gap of the films, UV-Vis spectra, at a diffuse reflectance mode, were recorded using a UV-Vis-NIR spectrometer (Varian Cary 5).

### Photoelectrochemical characterisation of the sulphurised films

The photoelectrochemical experiments for the sulphurised films prepared at different deposition potentials were performed by chronoamperometric measurements at − 0.315 V (the thermodynamic potential for the hydrogen evolution reaction at pH 2) in $N_2$-saturated solution composed of 0.5 mol $L^{-1}$ $Na_2SO_4$ and 1 mmol $L^{-1}$ 4-nitrophenol (electron scavenger) at pH 2. For this experiment, a three-electrode cell with a quartz window was employed. The sulphurised electrodeposits were frontside illuminated with a solar simulated light (Newport 66902, with a 150 W xenon lamp coupled to an AM 1.0 G filter) with radiance of 100 mW $cm^{-2}$.

The Mott-Schottky plots in the dark were obtained in the same solution used in the photoelectrochemical experiments. This experiment was carried out with a frequency of 1 kHz, amplitude of 10 mV and equilibrium time of 1 min prior to every applied potential. The applied potential ranged from $E_{ocp}$ to − 0.315 V.

## Results and discussion

### Electrochemical behaviour

The cyclic voltammogram profiles on the FTO of the individual solutions of 2 mmol $L^{-1}$ $Sn^{2+}$, 4 mmol $L^{-1}$ $Sb^{3+}$, the mixture of 2 mmol $L^{-1}$ $Sn^{2+}$ + 4 mmol $L^{-1}$ $Sb^{3+}$ and the supporting electrolyte, 0.1 mol $L^{-1}$ $KNa(C_4H_4O_6)$ pH 6, are depicted in Fig. 2.

Based on Fig. 2, the results show two cathodic peaks, $c_1$ and $c_2$ at ca. − 0.74 and − 1.25 V, respectively, for the $Sn^{2+}$ bath. According to Guaus and Torrent-Burgués [42], the occurrence of the two peaks suggests the existence of at least two stannous complexes in equilibrium with each other. Taking into consideration the tartrate speciation diagram, these complexes are likely the $[Sn(C_4H_5O_6)]^+$ and $[Sn(C_4H_4O_6)_2]^{2-}$ at pH 6 [42]. The stability constant for the former ($\log K_1 = 6.25$) is lower than for the latter complex ($\log \beta_2 = 11.48$) [42], meaning that the reduction of $Sn^{2+}$ ions coordinated with the tartrate anion $(C_4H_4O_6)^{2-}$ would be more difficult. Thus, the peak $c_1$ at less negative potential is attributed to the reduction of the $[Sn(C_4H_5O_6)]^+$ (Eq. 1) and the peak $c_2$ at more negative potential is assigned to the reduction of the $[Sn(C_4H_4O_6)_2]^{2-}$ species (Eq. 2).

$$[Sn(C_4H_5O_6)]^+_{(aq)} + 2e^- \rightarrow Sn_{(s)} + (C_4H_5O_6)^-_{(aq)} \quad (1)$$

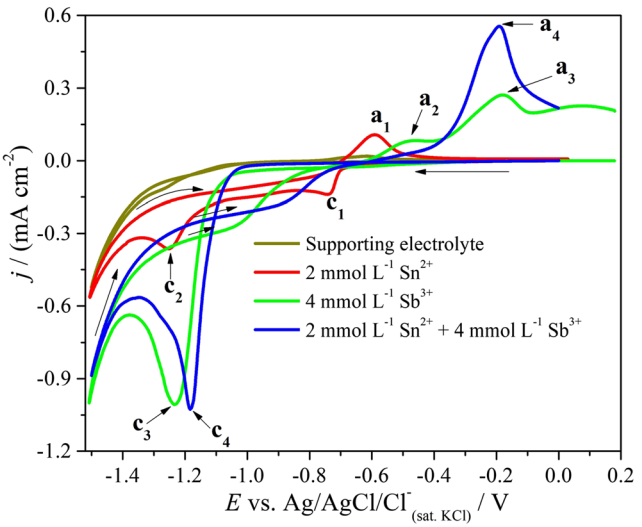


**Fig. 2** Cyclic voltammograms of FTO at a scan rate of 20 mV $s^{-1}$ for the 2 mmol $L^{-1}$ $Sn^{2+}$, 4 mmol $L^{-1}$ $Sb^{3+}$ and the mixture 2 mmol $L^{-1}$ $Sn^{2+}$ + 4 mmol $L^{-1}$ $Sb^{3+}$. The supporting electrolyte was 0.1 mol $L^{-1}$ $KNa(C_4H_4O_6)$ pH 6

$$\left[Sn(C_4H_4O_6)_2\right]^{2-}_{(aq)} + 2e^- \rightarrow Sn_{(s)} + 2(C_4H_4O_6)^{2-}_{(aq)} \quad (2)$$

In the reverse scan, scanning towards more positive potentials, an anodic peak $a_1$ is observed at ca. − 0.60 V, and it is ascribed to the oxidation process of Sn to $Sn^{2+}$.

The voltammogram for the $Sb^{3+}$ bath presents only one cathodic peak, $c_3$ at ca. − 1.23 V, which is related to the reduction reaction of the $[Sb_2(C_4H_4O_6)_2]^{2+}$ species [43], as shown by Eq. 3.

$$\left[Sb_2(C_4H_4O_6)_2\right]^{2+}_{(aq)} + 6e^- \rightarrow 2Sb_{(s)} + 2(C_4H_4O_6)^{2-}_{(aq)} \quad (3)$$

Sweeping in the reverse direction shows the dissolution processes indicated by the peaks $a_2$ (at ca. − 0.50 V) and $a_3$ (at ca. − 0.18 V). Such peaks could be attributed to the oxidation of Sb to $Sb^{3+}$, peak $a_2$, and followed by the oxidation of $Sb^{3+}$ to $Sb^{5+}$, $a_3$ [44].

Finally, for the bath containing the mixture of $Sn^{2+}$ + $Sb^{3+}$, only one cathodic peak $c_4$ (at ca. − 1.18 V) corresponds to the simultaneous reduction of $[Sn(C_4H_4O_6)_2]^{2-}$ and $[Sb_2(C_4H_4O_6)_2]^{2+}$ to form the binary compound SnSb, as indicated by Eq. 4.

$$2\left[Sn(C_4H_4O_6)_2\right]^{2-}_{(aq)} + \left[Sb_2(C_4H_4O_6)_2\right]^{2+}_{(aq)} + 10e^- \rightarrow 2SnSb_{(s)} + 6(C_4H_4O_6)^{2-}_{(aq)} \quad (4)$$

The anodic peak $a_4$ (at ca. − 0.19 V) indicates the process of anodic dissolution of the SnSb film formed in the forward scan. In addition, the dissolution profile of this binary bath changed compared to the individual baths, suggesting that the SnSb compound was indeed electrodeposited. Furthermore, the voltammograms of the baths $Sb^{3+}$ and the mixture of $Sn^{2+}$ and $Sb^{3+}$ presented crossovers between the curves for the forward and backward sweeps at ca. − 1.15 V and − 1.11, respectively, which indicates the occurrence of nucleation and growth process [45].

Comparing the deposition potential of the two elements, the $E([Sn(C_4H_4O_6)_2]^{2-}/Sn) \cong E([Sb_2(C_6H_4O_6)_2]^{2+}/Sb)$, meaning that the reduction process of the two species takes place concomitantly. For the other stannous complex reduction peak, the $E([Sn(C_4H_5O_6)]^{+}/Sn) > E([Sb_2(C_4H_4O_6)_2]^{2+}/Sb)$, which implies that the $[Sn(C_4H_5O_6)]^{+}$ reduction occurs first and then the reduction of the $[Sb_2(C_4H_4O_6)_2]^{2+}$.

According to the voltammetric study hereby presented, the potentials selected to electrodeposit the films were − 1.07, − 1.14 and − 1.18 V. The first and second chosen potentials correspond to the activation region and the half-wave potential, respectively, meaning that the electrodeposition is controlled by an activation process for the former and by a mix of activation and diffusion processes for the latter. The third chosen one refers only to a diffusion process. All of these films were deposited with a deposition charge density of − 332 mC $cm^{-2}$. For the sake of enhancing crystallinity and to obtain the sulphide phases Sn-S and Sb-S, the electrodeposited films at different deposition potentials were submitted to thermal treatment under a sulphur vapour atmosphere at 270 °C for 3 h. The unsulphured and sulphurised films were physically, optically and chemically characterised to evaluate the effect of the deposition potential on the microstructure, morphology and optoelectronic properties of the films. In addition, the photoelectroactivity was also investigated for the sulphurised films.

## Physical, chemical and optical characterisation

In order to unfold the microstructure of the unsulphured films obtained at different deposition potentials, X-ray diffraction (XRD) and Raman spectroscopy were conducted, and the results are presented in Fig. 3.

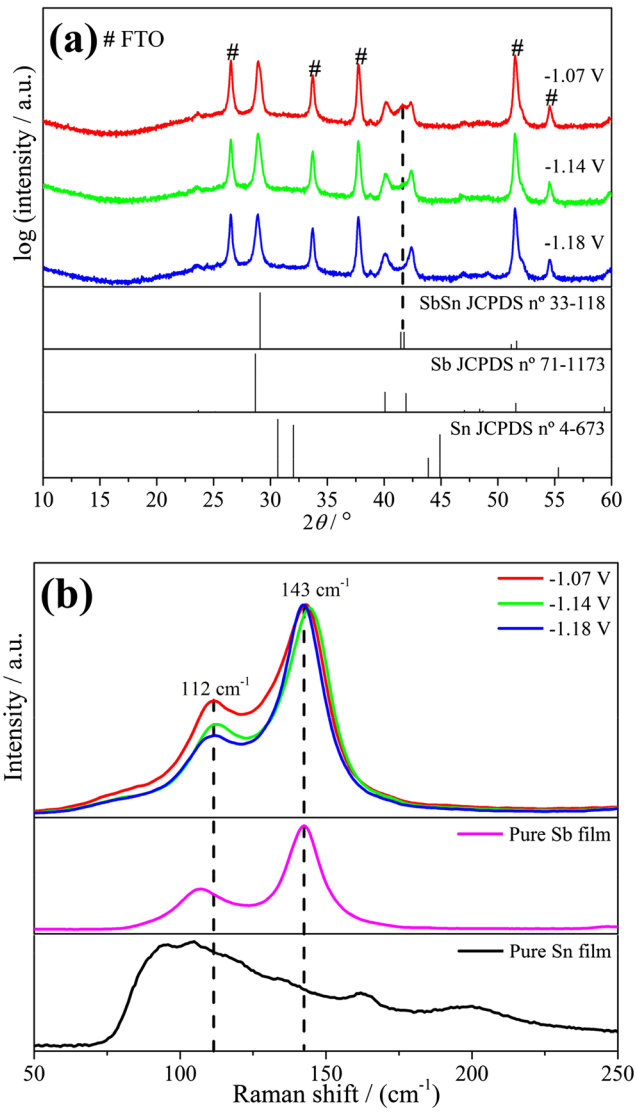


**Fig. 3** **a** XRD and **b** Raman spectra for the unsulphured films obtained at different deposition potentials. The diffraction peaks labelled with "#" are assigned to the FTO substrate

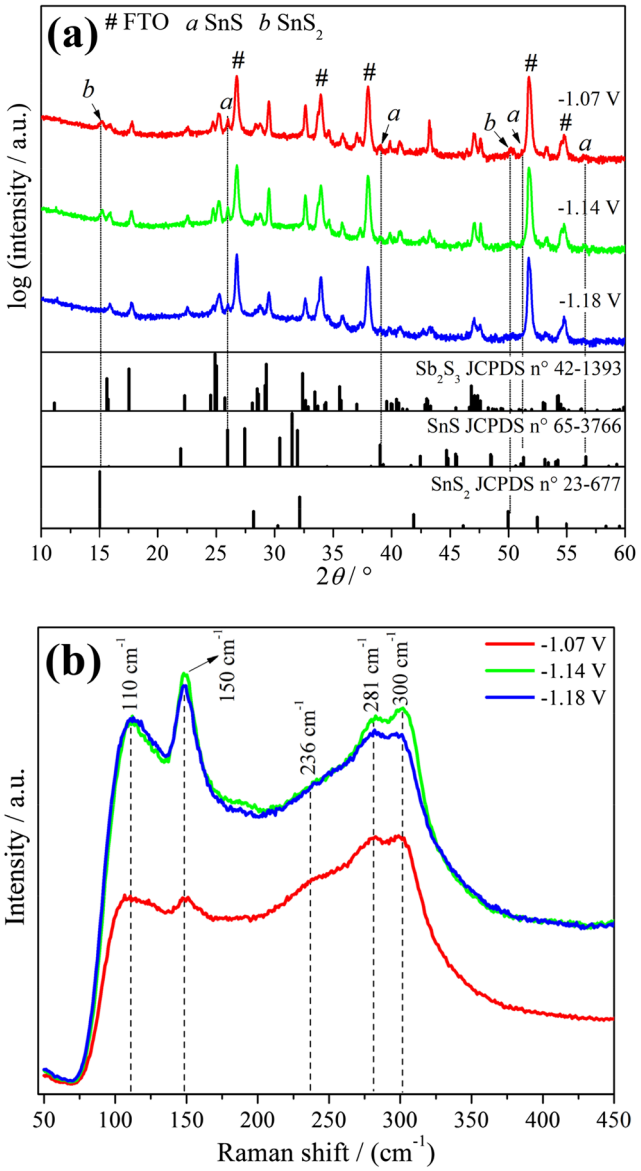


**Fig. 4** **a** XRD and **b** Raman spectra for the sulphurised films obtained at different deposition potentials. The diffraction peaks labelled with "#" are assigned to the FTO substrate

Firstly, the XRD data in Fig. 3a show diffraction peaks which indicate a crystalline nature in the electrodeposited films obtained at different potentials. The indexation of the diffraction peaks suggests the presence of Sb (JCPDS no. 71-1173 [46]) and SbSn phases (JCPDS no. 33-118 [47]), both having a rhombohedral crystal system. Although the main peak of SbSn overlaps with the main one of Sb, the broad peak around 42° (highlighted with a dashed line) is attributed to the SbSn phase, and the one at 40° to the Sb phase, confirming the existence of the SbSn and Sb phases. The results also suggest that as the deposition potential reaches more negative values, the film becomes more Sb-rich, as noted by the decrease in the peak at 42°.

Additional microstructural analysis was performed by Raman spectroscopy, as seen in Fig. 3, and the spectra show two bands centred at 112 and 143 $cm^{-1}$; these bands can be assigned to either the Sb [48, 49] or SbSn phase [50]. However, despite these phases have overlapping signals, the electrodeposited films have the two phases as confirmed by XRD (Fig. 3a) and the existence of the Sn-S and Sb-S phases once submitted to sulphurisation, which were proved by XRD and Raman analysis as depicted in Fig. 4.

In Fig. 4a, the unlabelled diffraction peaks of all the sulphurised films were indexed to the major phase, $Sb_2S_3$ (JCPDS no. 42-1393 [51]), which belongs to the orthorhombic crystal system. Additionally, all of the sulphurised films also presented some diffraction peaks, labelled as "*a*", at 26.0, 39.1°, 51.2 and 56.6° which were indexed to the SnS phase (JCPDS no. 65-3766, orthorhombic crystal system [52]). In turn, the sulphurised films electrodeposited at − 1.07 and − 1.14 V also had diffraction peaks, labelled as "*b*", at 15.1 and 50.1° which were indexed to the $SnS_2$ phase (JCPDS no. 23-677, trigonal crystal system [53]).

The Raman scattering in Fig. 4b shows bands at 281 and 300 $cm^{-1}$ related to the $Sb_2S_3$ phase with modes $A_g$ and $B_{1g}$, respectively [54]. The former and the latter bands are attributed to the antisymmetric stretching vibration $\nu_a$ (Sb-S) [54]. Another band related to the $Sb_2S_3$ phase was detected around 150 $cm^{-1}$, and it was ascribed to the vibration of Sb-Sb bonds in the $S_2Sb$-$SbS_2$ structural units [55]. The spectra also presented bands at 110 and 236 $cm^{-1}$, both having $A_g$ mode and assigned to the SnS phase [23, 56]. The main band of the $SnS_2$ phase, expected to be around 310 $cm^{-1}$ ($A_{1g}$) [57], has not been detected, which indicates that this is a minor phase. Furthermore, oxide phases have not been observed.

For the sake of estimating the energy of the optical (allowed) indirect band gap ($E_g$) of the sulphurised films which were electrodeposited at different potentials, Tauc plots were obtained and are presented in Fig. 5.

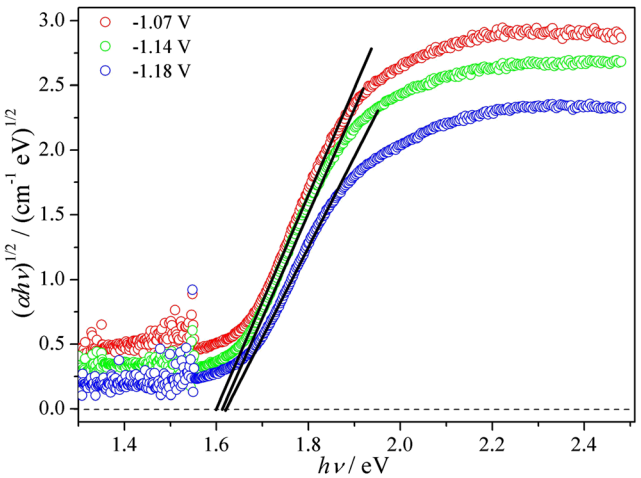


**Fig. 5** Tauc plots of the sulphurised films obtained at different deposition potentials

According to Fig. 5, the estimated $E_g$ values for an (allowed) indirect electronic transition of the sulphurised films electrodeposited at − 1.07, − 1.14 and − 1.18 V were 1.61 ± 0.06, 1.65 ± 0.01 and 1.60 ± 0.04 eV, respectively. These results are in accordance with the values reported in the literature for the $Sb_2S_3$ phase [4].

The examination of the surface morphology of the unsulphured and sulphurised films, which were electrodeposited at different deposition potential values, was conducted by scanning electron microscopy (SEM), and the results are shown in Fig. 6.

As can be seen from Fig. 6, the unsulphured film electrodeposited at − 1.07 V presented a morphology similar to parallelepiped-like clusters, and a dendritic-like morphology was observed for the films electrodeposited at − 1.14 and − 1.18 V. The morphology of the binary films seems to be less compact as the potential becomes more negative, which is a common behaviour; higher overpotential leads to a faster rate of deposition and, by consequence, generates structures with more nanostructured domains [58], such as dendrites or powders.

As shown in Fig. 6, the morphology dramatically changed after sulphurisation; the ones electrodeposited at − 1.07 and − 1.14 V showed rod-like nanoclusters that seem to be grown randomly throughout the surface of the film. The average widths of the rods presented on these films were 166 ± 15 nm and 151 ± 23 nm, respectively. Furthermore, in the base of the rods, a second structure resembling a corn flake-like morphology was also noticed in these films. On the other hand, the sulphurised film electrodeposited at − 1.18 V exhibited a higher density of needle-like structures and small rods all over the surface.

Lastly, the sulphurised materials electrodeposited at different potentials were evaluated in terms of their photoelectroactivity.

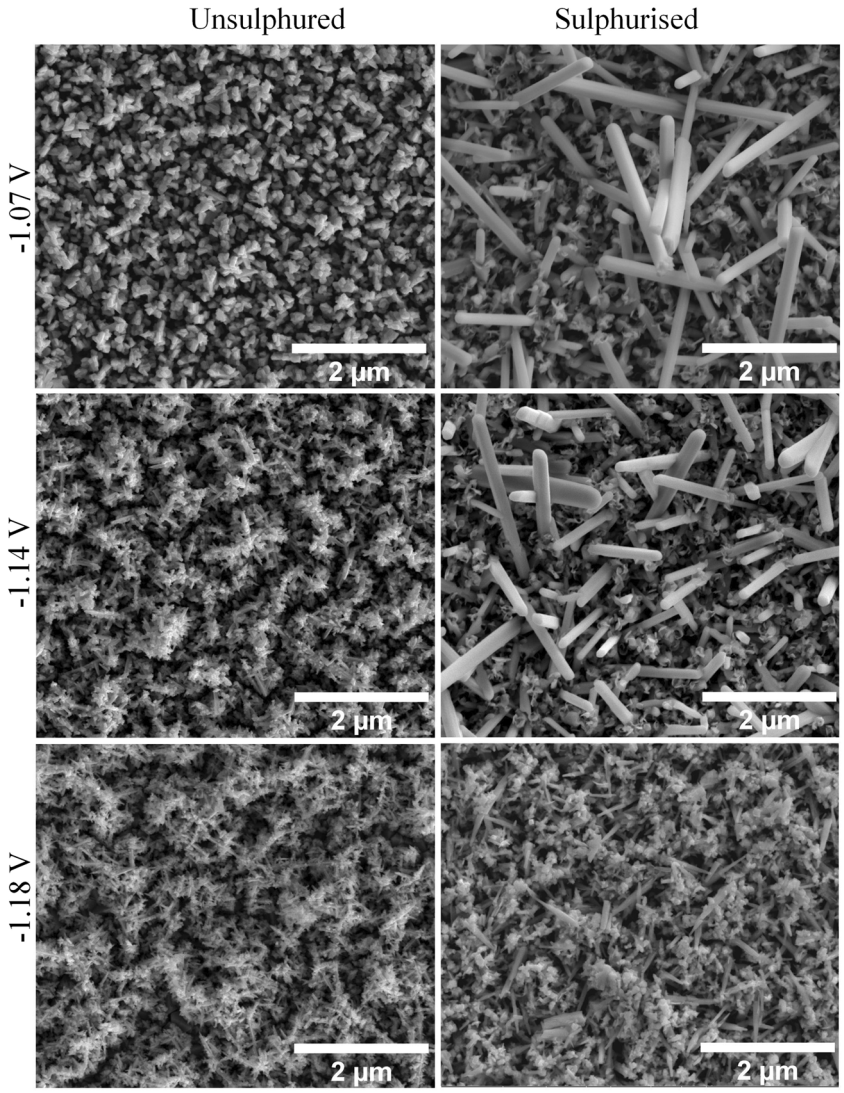


**Fig. 6** SEM micrographs of the unsulphured and sulphurised films obtained at different deposition potentials

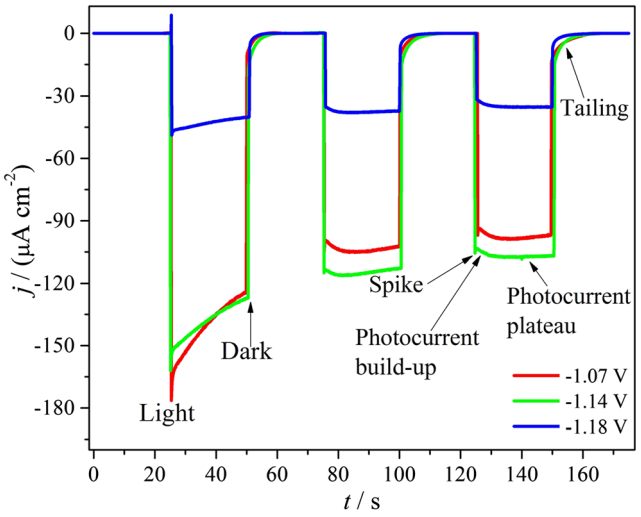


**Fig. 7** Photocurrent density transients at − 0.315 V vs. $Ag/AgCl/Cl^-_{(sat.\ KCl)}$ for the sulphurised films obtained at different deposition potentials. The electrolyte was 0.5 mol $L^{-1}$ $Na_2SO_4$ + 1 mmol $L^{-1}$ 4-nitrophenol at pH 2, and the illumination source was a solar light simulator, 100 mW $cm^{-2}$

## Photoelectrochemical assessment

The photoelectrochemical experiments carried out by chronoamperometry measurements polarised at − 0.315 V vs. $Ag/AgCl/Cl^-_{(sat.\ KCl)}$ and under a chopped solar light simulator are depicted in Fig. 7.

As seen in Fig. 7, all of the sulphurised electrodes are *p*-type semiconductors, because cathodic photocurrent densities were detected. This current density is attributed to the reduction of 4-nitrophenol to 4-aminophenol [59], as shown in Eq. 6, by the electrons photogenerated in the conduction band ($e^-_{CB}$) of the sulphurised films, seen in Eq. 5 [60]. As it is an electron scavenger and can minimise superficial recombination and photodegradation of the films, 4-nitrophenol was chosen.

$$h\nu \longrightarrow h^+_{VB} + e^-_{CB} \tag{5}$$

where $h\nu$ represents the photon energy that creates holes in the valence band (VB), $h^+_{VB}$, and electrons in the conduction band (CB), $e^-_{CB}$.

Under illumination, the photocurrent density transient profile presented an exponential decay of the photocurrent density from slight spikes in all the sulphurised electrodeposited films, and that is associated with electron-hole recombination at the semiconductor surface [61]. It is also noticeable when the light is on a slow photocurrent density build-up before reaching the steady-state photocurrent density plateau. Such phenomenon is ascribed to the existence of traps in the band gap which first need to be filled with photogenerated charge carriers before reaching the steady-state condition [61]. Moreover, once the light is shut off, the tailing of the transient is observed in all of the films. This may be attributed to the capture of non-equilibrium charge carriers by band-tail localised states which can undergo a recombination process afterward [62].

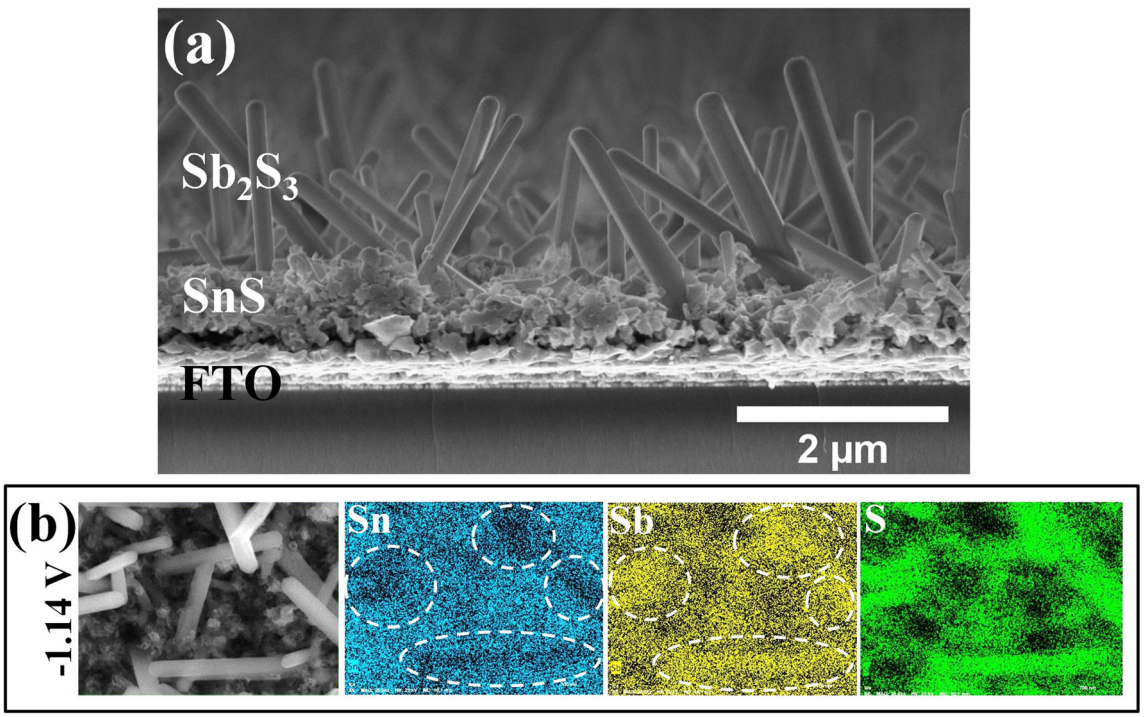


**Fig. 8** **a** Cross-sectional image and **b** EDS elemental mapping images of the sulphurised film obtained at − 1.14 V. From left to right, the mapping for Sn, Sb and S are shown, respectively

In terms of photocurrent density values, the sulphurised film electrodeposited at − 1.14 V presented the highest photocurrent density, which was − 118.7 ± 11.0 μA $cm^{-2}$, whereas the electrodeposited one at − 1.07 V had a photocurrent density of − 85.2 ± 22.5 μA $cm^{-2}$. The lowest photocurrent density (− 27.8 ± 7.1 μA $cm^{-2}$) was achieved for the sulphurised film electrodeposited at − 1.18 V. The differences in photocurrent density values may probably be linked to the films' morphology. Comparing these results with the SEM images in Fig. 6, the highest photocurrent density values occurred for the sulphurised films in which the morphology presented a rod structure.

In addition to the morphology, another important aspect to bring to light is the role of the sulphide phases (SnS and $Sb_2S_3$), identified in the sulphurised films by XRD and Raman data (Fig. 4), plays in the photoelectroactivity. We believe that the SnS and $Sb_2S_3$ phases formed a heterostructure $SnS/Sb_2S_3$ which facilitated minority carriers' separation and transportation and, consequently, improved the photocurrent. In order to verify our hypothesis, we firstly obtained a cross-sectional SEM image and energy-dispersive X-ray spectroscopy (EDS) elemental mapping images for the sulphurised film which resulted at the highest photocurrent density value (− 1.14 V). The results are shown in Fig. 8.

The cross-sectional image in Fig. 8a shows that the film is comprised of two structures: Just above the FTO layer, sort of globular particles are forming a compact layer with a mean thickness of 576 ± 55 nm. The second structure, which stands on top of the first one, features a rod structure with a mean height of 1.9 ± 0.2 μm. Aiming to chemically characterise the two structures, EDS elemental mapping images were obtained; the results, as shown in Fig. 8b, indicate that the rods are $Sb_2S_3$-rich as the rod structures seen in the SEM image showed a rod-shaped black contour (signalled by dashed circles) in the Sn mapping and were brighter in the Sb mapping. The occurrence of such a structure for $Sb_2S_3$ is quite common and is well known in literature [19, 63, 64]. The other regions not signalled by dashed circles in the Sn mapping appears to be brighter than in the Sb mapping, indicating then that the compact layer might be SnS-rich.

To further back up our heterostructure hypothesis, elemental films of Sn and Sb were prepared at the optimal electrodeposition condition (− 1.14 V and a deposition charge density of − 332 mC $cm^{-2}$) and sulphurised at 270 °C per 3 h afterward. The elemental unsulphured and sulphurised films were characterised by XRD (Figs. S1 and S3) and Raman (Figs. S2 and S4); the results showed that the sulphurised Sn film is made up of SnS and $SnS_2$ phases, whilst $Sb_2S_3$ phase was identified for the sulphurised Sb films. As shown in Fig. S5, the estimated optical (allowed) indirect $E_g$ for the sulphurised Sb was 1.67 eV which is in accordance with the value for the $Sb_2S_3$ phase [4], whilst for the sulphurised Sn was 1.18 eV. Such value is assigned to the SnS phase [6]. Further characterisation of these materials can be found in the Support Information.

The photoelectroactivity of the sulphurised Sn and Sb films is presented in Fig. 9a. The sulphurised SbSn film is also presented for the sake of comparison.

According to Fig. 9a, the sulphurised Sn and Sb films are also *p*-type semiconductors. Comparing the photocurrent density values, the cathodic photocurrent density of the sulphurised Sn (− 2.5 μA $cm^{-2}$) and Sb (− 12.2 μA $cm^{-2}$) were overwhelmingly lower in comparison to the sulphurised SbSn (− 118.7 μA $cm^{-2}$). This substantially improved photocurrent density of the sulphurised SbSn film compared to the binary ones is linked to nanostructuring of the film (it

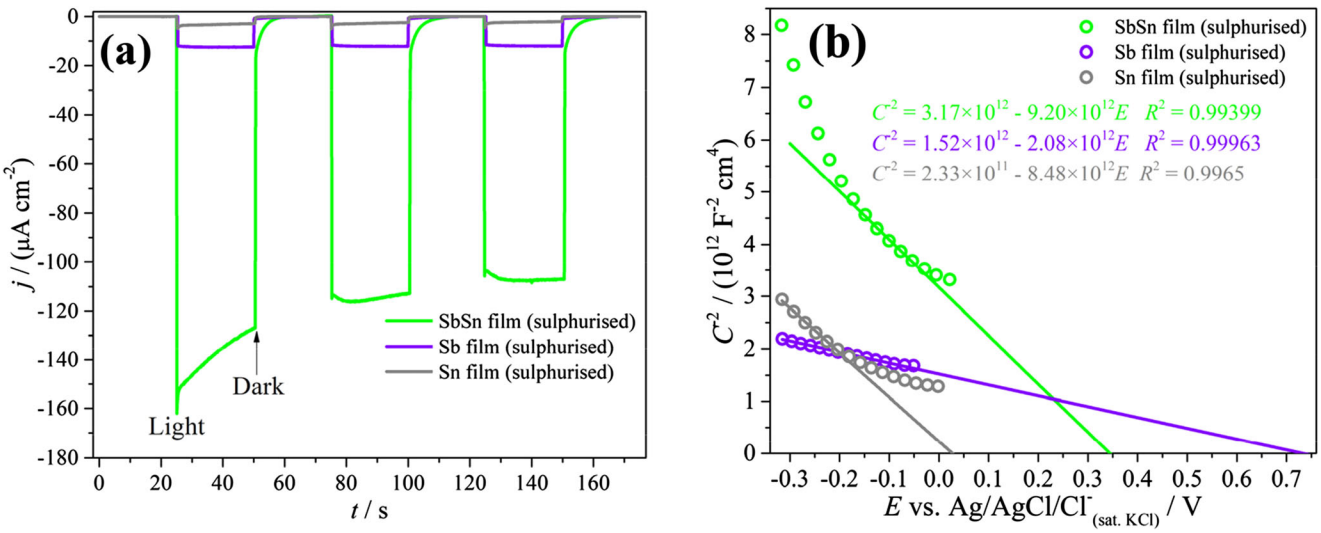


**Fig. 9** **a** Photocurrent density transient at − 0.315 V vs. $Ag/AgCl/Cl^-_{(sat.\ KCl)}$ under chopped solar light simulator (100 mW $cm^{-2}$) and **b** Mott-Schottky plots in the dark of the sulphurised Sn, Sb and SbSn films. The electrolyte was 0.5 mol $L^{-1}$ $Na_2SO_4$ + 1 mmol $L^{-1}$ 4-nitrophenol at pH 2

**Table 1** $E_g$, $E_{fb}$, $E_v$, $E_c$ and $N_D$ values for the sulphurised Sn, Sb and SbSn films

| Sample | $E_g$[a]/eV | $E_{fb}$[b]/V vs. RHE | $E_v$[b]/eV vs. vacuum | $E_c$[b]/eV vs. vacuum | $N_D$/cm$^{-3}$ |
|---|---|---|---|---|---|
| Sb film (sulphurised) | 1.67 | 1.02 | − 5.46 | − 3.79 | $1.8 \times 10^{19}$ |
| Sn film (sulphurised) | 1.18 | 0.32 | − 4.76 | − 3.58 | $3.3 \times 10^{18}$ |
| SbSn film (sulphurised) | 1.65 | 0.63 | − 5.07 | − 3.42 | $6.1 \times 10^{18}$ |

[a] Indirect (allowed) electron transition

[b] Parameters obtained in an electrolyte of 0.5 mol L$^{-1}$ $Na_2SO_4$ + 1 mmol L$^{-1}$ 4-nitrophenol pH 2

facilitates carriers' transportation [65]) as well as the existence of an SnS/$Sb_2S_3$ heterostructure which backs up our hypothesis.

In order to confirm and validate our hypothesis, band edge positions for the sulphurised Sn, Sb and SbSn films were obtained from the Mott-Schottky analysis (Fig. 9b) and (allowed) indirect $E_g$ values as described in the Support Information. According to this study, the values of flat band potential ($E_{fb}$), carrier density ($N_D$), valence band maximum energy ($E_v$) and conduction band minimum energy ($E_c$) are summarised in Table 1.

At last, the band diagram (Fig. 10) for the SnS and $Sb_2S_3$ films was constructed using the band edge data listed in Table 1.

The band diagram in Fig. 10 shows that the valence band maximum (VBM) and conduction band minimum (CBM) of the $Sb_2S_3$ film are shifted towards lower energy versus vacuum, compared to the SnS film. These band energy positions favour the transportation of the photogenerated minority carriers (the electrons) from the CBM-SnS to the CBM-$Sb_2S_3$ and consequent reduction of the 4-nitrophenol. Furthermore, photogenerated majority carriers (holes) are transported from the VBM-$Sb_2S_3$ to the VBM-SnS and then to the inner circuit. As a direct consequence of these band configurations, cathodic photocurrent density is enhanced (see Fig. 9a) as more photogenerated electrons are reaching the surface of the sulphurised SnSb to reduce the 4-nitrophenol.

## Conclusions

To summarise, a simple approach has been developed to obtain the SnS/$Sb_2S_3$ heterostructure using the electrodeposition of the binary system (SnSb) followed by sulphurisation under a sulphur vapour atmosphere. The optical and physical properties as a function of the deposition potential of SnSb were fully assessed before and after sulphurisation. Regarding the photoelectrochemical evaluation for the reduction of 4-nitrophenol (an electron scavenger), the sulphurised binary film electrodeposited at − 1.14 V promoted the highest photocurrent density, which was − 118.7 ± 11.0 μA cm$^{-2}$. In comparison to this, the individual sulphurised films of Sn and Sb prepared at the optimal deposition potential (− 1.14 V) presented reduced photocurrent density. Further studies based on band diagrams of the SnS and $Sb_2S_3$ films showed that the CBM-$Sb_2S_3$ and VBM-$Sb_2S_3$ energies are lower than the CBM-SnS and VBM-SnS energies. As a result, the photocurrent density enhancement is not only due to the nanostructuring of the film, but

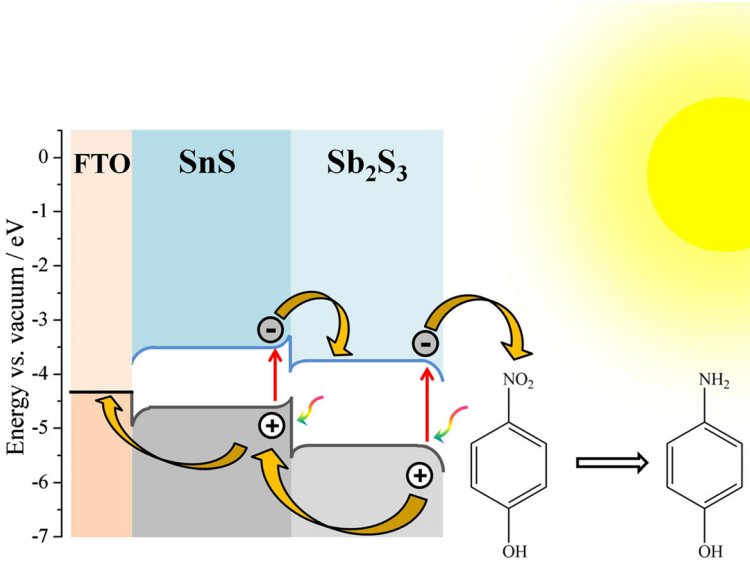


**Fig. 10** Band diagram for the SnS and $Sb_2S_3$ films obtained from Mott-Schottky and (allowed) indirect $E_g$ values

may be also caused by the formation of the type II heterostructure $SnS/Sb_2S_3$ in the sulphurised binary film. In light of these results, the new nanostructured and heterostructured $SnS/Sb_2S_3$ system presented superlative optoelectronic properties and photoelectroactivity for a future application in PEC, as a photocathode, and met the requirements for use as an absorber layer in PV devices.

**Funding information** This study received financial support from São Paulo Research Foundation (FAPESP) grants: #2016/12681-0 (M.A.A), #2018/03156-5 (F.W.S.L.), #2013/07296-2 (CEPID/CDMF) and #2018/16401-8 (L.H.M.).

## References

1. Khan MA, Ahmed A, Ali N, Iqbal T, Khan AA, Ullah M, Shafique M (2016) Improved optical properties of tin antimony sulphide thin films for photovoltaics. Am J Mater Sci Eng 4(1):1–6
2. Cho JY, Sinha S, Gang MG, Heo J (2019) Controlled thickness of a chemical-bath-deposited CdS buffer layer for a SnS thin film solar cell with more than 3% efficiency. J Alloys Compd 796:160–166
3. Wu Y, Wei T, An X, Liu L-M (2019) Colloidal synthesis of SnS nanocrystals with dimension-dependent photoelectrochemical properties. New J Chem 43:7457–7462
4. Lei H, Chen J, Tan Z, Fang G (2019) Review of recent progress in antimony chalcogenide-based solar cells: materials and device. Sol RRL 3:1900026
5. DeAngelis AD, Kemp KC, Gaillard N, Kim KS (2016) Antimony (III) sulfide thin films as a photoanode material in photocatalytic water splitting. ACS Appl Mater Interfaces 8(13):8445–8451
6. Banai RE, Horn MW, Brownson JRS (2016) A review of tin (II) monosulfide and its potential as a photovoltaic absorber. Sol Energy Mater Sol Cells 150:112–129
7. Pejjai B, Reddy VRM, Gedi S, Park C (2017) Status review on earth-abundant and environmentally green Sn-X (X=Se, S) nanoparticle synthesis by solution methods for photovoltaic applications. Int J Hydrog Energy 42:2790–2831
8. Huang P-C, Shen Y-M, Brahma S, Shaikh MO, Huang J-L, Wang S-C (2017) $SnS_x$ (x = 1, 2) nanocrystals as effective catalysts for photoelectrochemical water splitting. Catalysts 7:252
9. Burton LA, Whittles TJ, Hesp D, Linhart WM, Skelton JM, Hou B, Webster RF, O'Dowd G, Reece C, Cherns D, Fermin DJ, Veal TD, Dhanak VR, Walsh A (2016) Electronic and optical properties of single crystal $SnS_2$: an earth-abundant disulfide photocatalyst. J Mater Chem A 4:1312–1318
10. Whittles TJ, Burton LA, Skelton JM, Walsh A, Veal TD, Dhanak VR (2016) Band alignments, valence bands, and core levels in the tin sulfides SnS, $SnS_2$, and $Sn_2S_3$: experiment and theory. Chem Mater 28(11):3718–3726
11. Bouroushian M (2010) Electrochemistry of metal chalcogenides. Springer
12. Yang F, Xi J, Gan L-Y, Wang Y, Lu S, Ma W, Cai F, Zhang Y, Cheng C, Zhao Y (2016) Improved charge transfer and photoelectrochemical performance of $CuI/Sb_2S_3/TiO_2$ heterostructure nanotube arrays. J Colloid Interface Sci 464:1–9
13. Medina-Montes MI, Montiel-González Z, Paraguay-Delgado F, Mathews NR, Mathew X (2016) Structural, morphological and spectroscopic ellipsometry studies on sputter deposited $Sb_2S_3$ thin films. J Mater Sci Mater Electron 27(9):9710–9719
14. Baek I-H, Pyeon JJ, Song YG, Chung T-M, Kim H-R, Baek S-H, Kim J-S, Kang C-Y, Choi J-W, Hwang CS, Han JH, Kim SK (2017) Synthesis of SnS thin films by atomic layer deposition at low temperatures. Chem Mater 29:8100–8110
15. Jo H-J, Mun YH, Kim JS (2018) Determination of carrier lifetimes in organic-inorganic hybrid solar cells based on $Sb_2S_3$ by using the time-resolved photocurrent. J Korean Phys Soc 72(6):709–715
16. Kim J, Kim J, Yoon S, Kang J, Jeon C-W, Jo W (2018) Single phase formation of SnS competing with $SnS_2$ and $Sn_2S_3$ for photovoltaic applications: optoelectronic characteristics of thin-film surfaces and interfaces. J Phys Chem C 122(6):3523–3232
17. Gao C, Huang J, Li H, Sun K, Lai Y, Jia M, Jiang L, Liu F (2019) Fabrication of $Sb_2S_3$ thin films by sputtering and post-annealing for solar cells. Ceram Int 45:3044–3051
18. Yu D, Li Q, Wei A, Zhao Y, Liu J, Xiao Z (2019) Synthesis and characterization of the ultra-thin SnS flakes and the micron-thick SnS crystals by chemical vapor deposition. J Mater Sci Mater Electron 30:10879–10885
19. Murtaza G, Akhtar M, Malik MA, O'Brien P, Revaprasadu N (2015) Aerosol assisted chemical vapor deposition of $Sb_2S_3$ thin films: environmentally benign solar energy material. Mater Sci Semicond Process 40:643–649
20. Jamali-Sheini F, Cheraghizade M, Yousefi R (2016) SnS nanosheet films deposited via thermal evaporation: the effects of buffer layers on photovoltaic performance. Sol Energy Mater Sol Cells 154:49–56
21. Reddy NK, Reddy KTR (2006) Optical behaviour of sprayed tin sulphide thin films. Mater Res Bull 41:414–422
22. Boughalmi R, Boukhachem A, Kahlaoui M, Maghraoui H, Amlouk M (2014) Physical investigations on $Sb_2S_3$ sprayed thin film for optoelectronic applications. Mater Sci Semicond Process 26:593–602
23. Mahdi MS, Ibrahim K, Hmood A, Ahmed NM, Mustafa FI (2017) Control of phase, structural and optical properties of tin sulfide nanostructured thin films grown via chemical bath deposition. J Electron Mater 46(7):4227–4235
24. Krishnan B, Arato A, Cardenas E, Das RTK, Castillo GA (2008) On the structure, morphology, and optical properties of chemical bath deposited $Sb_2S_3$ thin films. Appl Surf Sci 254:3200–3206
25. Zhou Y, Wang L, Chen S, Qin S, Liu X, Chen J, Xue D-J, Luo M, Cao Y, Cheng Y, Sargent EH, Tang J (2015) Thin-film $Sb_2Se_3$ photovoltaics with oriented one-dimensional ribbons and benign grain boundaries. Nat Photonics 9:409–415
26. Lucas FWS, Mascaro LH (2018) Electrochemical deposition of the single phase $Tl_xCu_{3-x}Se_2$ thin films. J Braz Chem Soc 0(0):1–8
27. Niknia F, Jamali-Sheini F, Yousefi R, Cheraghizade M (2018) Effect of thickness on the optoelectronic properties of electrodeposited nanostructured SnS films. Opt Quant Electron 50:339
28. Cheng S, Chen G, Chen Y, Huang C (2006) Effect of deposition potential and bath temperature on the electrodeposition of SnS film. Opt Mater (Amst) 29:439–444
29. Kafashan H, Azizieh M, Balak Z (2017) Electrochemical synthesis of nanostructured se-doped SnS: effect of Se-dopant on surface characterizations. Appl Surf Sci 410:186–195
30. Niknia F, Jamali-Sheini F, Yousefi R (2016) Examining the effect of Zn dopant on physical properties of nanostructured SnS thin film by using electrodeposition. J Appl Electrochem 46:323–330
31. Zhang S, Cheng S, Jia H, Zhou H (2012) Preparation and characterization of aluminium-doped SnS thin films. Adv Mater Res 418-420:712–716
32. Garcia RGA, Avendaño CAM, Pal M, Delgado FP, Mathews NR (2016) Antimony sulfide ($Sb_2S_3$) thin films by pulse electrodeposition: effect of thermal treatment on structural, optical and electrical properties. Mater Sci Semicond Process 44:91–100

33. Yesugade NS, Lokhande CD, Bhosale CH (1995) Structural and optical properties of electrodeposited $Bi_2S_3$, $Sb_2S_3$ and $As_2S_3$ thin films. Thin Solid Films 263:145–149
34. Sarangi CK, Baral A, Panigrahi J, Sanjay K, Subbaiah T, Mishra BK (2014) Electro-crystallization of antimony from acidic and alkaline baths in diaphragm-less cell. Adv Mater Res 828:65–72
35. Cheng W, Singh N, Elliott W, Lee J, Rassoolkhani A, Jin X, McFarland EW, Mubeen S (2018) Earth-abundant tin sulfide-based photocathodes for solar hydrogen production. Adv Sci 5: 1700362
36. Vequizo JJM, Yokoyama M, Ichimura M, Yamakata A (2016) Enhancement of photoelectrochemical activity of SnS thin-film photoelectrodes using $TiO_2$, $Nb_2O_5$, and $Ta_2O_5$ metal oxide layers. Appl Phys Express 9:67101
37. Cai Q, Liu Z, Han C, Tong Z, Ma C (2019) $CuInS_2/Sb_2S_3$ heterostructure modified with noble metal co-catalyst for efficient photoelectrochemical water splitting. J Alloys Compd 795:319–326
38. Jiang L, Chen J, Wang Y, Pan Y, Xiao B, Ouyang N, Liu F (2018) $Sb_2O_3/Sb_2S_3$ Heterojunction composite thin film photoanode prepared via chemical bath deposition and post-sulfidation. J Electrochem Soc 165(16):H1052–H1058
39. Bera S, Roy A, Guria AK, Mitra S, Pradhan N (2019) Insights of diffusion doping in formation of dual-layered material and doped heterostructure SnS–Sn:$Sb_2S_3$ for sodium ion storage. J Phys Chem Lett 10(5):1024–1030
40. Costa MB, Lucas FWS, Mascaro LH (2019) Electrodeposition conditions effect $Sb_2Se_3$ thin-film properties. ChemEletroChem 6: 2937–2944
41. Lucas FWS, Lima ARF, Mascaro LH (2014) The electrodeposition of Ga-doped $CuInSe_2$ thin film in the presence of triton 100-X. Electrochim Acta 147:47–53
42. Guaus E, Torrent-Burgués J (2005) Tin-zinc electrodeposition from sulphate-tartrate baths. J Electroanal Chem 575(2):301–309
43. Garnica MC, Arcos J, Palacios JL (1990) Electroanalytical study of the reduction of Sb (III) in tartrate medium. Anal Lett 23(2):351–363
44. Bratsch SG (1989) Standard electrode potentials and tempearature coefficients in water at 298.15 K. J Phys Chem Ref Data 18:1–21
45. Taguchi ADS, Bento FR, Mascaro LH (2008) Nucleation and growth of tin-zinc electrodeposits on a polycrystalline platinum electrode in tartaric acid. J Braz Chem Soc 19(4):727–733
46. Schiferl D (1977) 50-kilobar gasketed diamond anvil cell for single-crystal x-ray diffractometer use with the crystal structure of Sb up to 26 kilobars as a test problem. Rev Sci Instrum 48(1):24–30
47. Morris MC, McMurdie HF, Evans EH, Paretzkin B, de Groot J (1979) Standard X-ray diffraction powder patterns section 16 - data for 86 substances
48. Fischer A, Scheidt E-W, Scherer W, Benson DE, Wu Y, Eklöf D, Häussermann U (2015) Thermal and vibrational properties of thermoelectric ZnSb: exploring the origin of low thermal conductivity. Phys Rev B 91:224309
49. Drewett NE, Gómez-Cámer JL, Acebedo B, Galceran M, Rojo T (2017) Sol-gel synthesized antimony anodes for sodium-ion batteries: identifying key parameters for optimization. Batteries 3:20
50. Lakshmi D, Nalini B, Sivaraj P, Jayapandi S (2017) Electro analytical studies on indium incorporated SnSb alloy anode for Li-ion batteries. J Electroanal Chem 801:459–465
51. Bayliss P, Nowacki W (1972) Refinement of the crystal structure of stibinite, $Sb_2S_3$. Z Krist 135:308–315
52. Wiedemeier H, von Schnering HG (1978) Refinement of the structures of GeS, GeSe, SnS and SnSe. Z Krist 148:295–303
53. Swanson HE, McMurdie HF, Morris MC, Evans EH, Paretzkin B (1971) Standard X-ray diffraction powder patterns section 9 - data for 63 substances
54. Medles M, Benramdane N, Bouzidi A, Sahraoui K, Miloua R, Desfeux R, Mathieu C (2014) Raman and optical studies of spray pyrolysed $Sb_2S_3$ thin films. J Optoelectron Adv Mater 16(5–6): 726–731
55. Horoz S, Koc H, Sahin Ö (2017) Investigation of structural, optical and photovoltaic properties of $Sb_2S_3$ thin films. Cumhur Sci J 38-3: 588–593
56. Sohila S, Rajalakshmi M, Ghosh C, Arora AK, Muthamizhchelvan C (2011) Optical and Raman scattering studies on SnS nanoparticles. J Alloys Compd 509:5843–5847
57. Gurnani C, Hawken SL, Hector AL, Huang R, Jura M, Levason W, Perkins J, Reid G, Stenning GBG (2018) Tin (IV) chalcogenoether complexes as single source precursors for the chemical vapour deposition of $SnE_2$ and SnE (E = S, Se) thin films. Dalton Trans 47: 2628–2637
58. Paunovic M, Schlesinger M (2006) Fundamentals of electrochemical deposition. John Wiley & Sons, Hoboken
59. Devi LB, Mandal AB (2013) Self-assembly of Ag nanoparticles using hydroxypropyl cyclodextrin: synthesis, characterisation and application for the catalytic reduction of p-nitrophenol. RSC Adv 3: 5238–5253
60. Peter LM (1990) Dynamic aspects of semiconductor photoelectrochemistry. Chem Rev 90:753–769
61. Rohloff M, Cosgun S, Massué C, Lunkenbein T, Senyshyn A, Lerch M, Fischer A, Behrens M (2019) The role of synthesis conditions for structural defects and lattice strain in β-TaON and their effect on photo- and photoelectrocatalysis. Z Naturforsch 74(1):71–83
62. Kumar P, Thangaraj R (2009) Effect of Sn addition on the photoconductivity of narrow-gap $Sb_2Se_3$ films. Philos Mag Lett 89(4): 241–249
63. Shuai X, Shen W (2012) A facile chemical conversion synthesis of $Sb_2S_3$ nanotubes and the visible light-driven photocatalytic activities. Nanoscale Res Lett 7:199
64. Alemi A, Hanifehpour Y, Joo SW (2011) Synthesis and characterization of $Sb_2S_3$ nanorods via complex decomposition approach. J Nanomater 2011:1–6
65. Peter LM, Gurudayal WLH, Abdi FF (2018) Understanding the role of nanostructuring in photoelectrode performance for light-driven water splitting. J Electroanal Chem 819:447–458